INSTITUTE OF PHYSICS PUBLISHING MEASUREMENT SCIENCE AND TECHNOLOGY
Meas. Sci. Technol. **15** (2004) 451–459 PII: S0957-0233(04)69214-9

Calibrated measurement of the behaviour of mechanical junctions from micrometre to subnanometre scale: the friction force scanner

Daniel Sidobre[1] **and Vincent Hayward**[2,3]

[1] Laboratoire d'Analyse et d'Architecture des Systèmes, 7 avenue du Colonel Roche, 31077 Toulouse, France
[2] Centre for Intelligent Machines, 3480 University Street, McGill University, Montreal, H3A 2A7, Canada

E-mail: daniel.sidobre@laas.fr and hayward@cim.mcgill.ca

Received 16 September 2003, in final form 20 November 2003, accepted for publication 8 December 2003
Published 20 January 2004
Online at stacks.iop.org/MST/15/451 (DOI: 10.1088/0957-0233/15/2/020)

Abstract
We describe an instrument called a friction force scanner (FFS) able to perform calibrated measurements of the behaviour of mechanical junctions with more than four orders of magnitude of resolution for both displacement and force. A probe carrier is suspended by fibres in an arrangement that provides exactly two degrees of freedom of motion. The suspension makes it possible to measure the carrier displacement by interferometry. A novel differential electrostatic actuator with linear response mounted on the carrier was used to precisely determine the force experienced by a junction. The single-stage design is easily calibrated and can be used for force measurement and scanning, allowing the study of friction at multiple length scales. Measurements involving mica–mica and steel–steel junctions are reported while using the instrument in open loop.

Keywords: friction force instruments, atomic force microscopy, atomic scale friction, electrostatic actuators, fibre suspensions

1. Introduction

The mechanisms that form the basis of friction remain largely unexplained. Several models have been proposed in the recent years, appealing notably to phenomena involving phonons [1], 'third bodies' [2], and recently fracture creation and healing [3]. This provides motivation for developing instruments capable of detailed measurements of the behaviour of mechanical junctions. Such instruments are also useful for applications in tribology and other fields [4–6].

Common designs are related to atomic force microscopy [7, 8], whereby the behaviour of a junction is observed by measuring the deformations of a flexible cantilevered probe interacting with a sample. Recently, an instrument was designed to investigate the behaviour of junctions using a probe and a sample, each supported by leaf springs arranged orthogonally [9]. Another instrument is the interfacial force microscope that uses electrostatically driven feedback to create rigid displacement [10]. Magnetically activated probe designs that can boost sensitivity and decoupling of normal and tangential measurements have also been described [11]. Most instruments balance the net force experienced at a junction by strain forces resulting from the deformation of flexures. Measurement of displacement [12], together with calibration of the flexural response, makes it then possible to evaluate the net force at the junction.

In this paper, we describe an instrument called the friction force scanner (FFS) which uses electrostatic energy instead of strain energy. It has a single stage and yet achieves a

[3] Author to whom any correspondence should be addressed.

very large range. The probe interacting with the sample is mounted on a carrier supported by a fibre suspension which has several advantages over previous designs. The suspension provides nearly perfect kinematic guidance in order to reduce the number of degrees of freedom to exactly two, simplifying modelling and calibration. The precise guidance makes it possible to detect the probe movements by interferometry. It also has a displacement range sufficient to permit the same stage to be used for interaction force measurement and scanning at multiple scales, hence taking advantage of the range of the interferometer. By design, the tunable suspension compliance is linear over the operating range, and parasitic terms due to mechanical hysteresis and gravity are eliminated. The suspended probe carrier has two electrostatic comb actuators acting in the normal and the tangential directions. A novel linearized differential electrostatic actuator provides calibrated force measurement over the entire operating range.

The instrument was operated in the quasi-static range. Without controlling environmental factors other than taking ordinary precautions, it achieved better than 2×10^{-7} N of force resolution in a $\pm 2 \times 10^{-4}$ N range. Position was measured by a commercially available interferometer (precision optical displacement sensor or PODS from MPB Technologies Inc., Montreal) that gives 0.1 nm of tangential displacement resolution [13]. The movement range was larger than 1 μm; thus we could investigate the behaviour of mechanical junctions over four orders of magnitude for force and displacement simultaneously.

2. Instrument design

2.1. Suspension

Suspensions can be realized with leaves or with fibres. Leaves are often used in pairs to create the approximation of a sliding joint. However, the compliance of a suspension based on leafs in a desired direction depends on stiffness in the other directions, so design tradeoffs are introduced. In addition, compliance varies with deflection due to the bending shape mode, complicating calibration.

The suspension must provide two directions of movement corresponding to the normal and tangential relative displacements of two samples. Therefore it must create four constraints, one in translation and three in rotation. Fibres seem unsuitable at first sight because they cannot be used to create these constraints simultaneously. To see that, consider that a single fibre defines a translational constraint at one point. Several fibres parallel to one another also create one translational constraint but two rotational constraints as well. Two different fibre directions are required to constrain three rotations; therefore the problem has no solution. It is nevertheless possible to achieve an arbitrarily close approximation. Referring to figure 1(a), a carrier holding a probe is suspended with three parallel fibres to constrain it to planar motions. A fourth orthogonally crossing fibre defines a centre of rotation. This approximates two translational freedoms at the tip. It is the tension of the fibres which determines the suspension compliance. Section 2.3 further describes the mechanism which was implemented to provide for tunable tension and for a linear compliant behaviour over a wide range of suspension deflections.

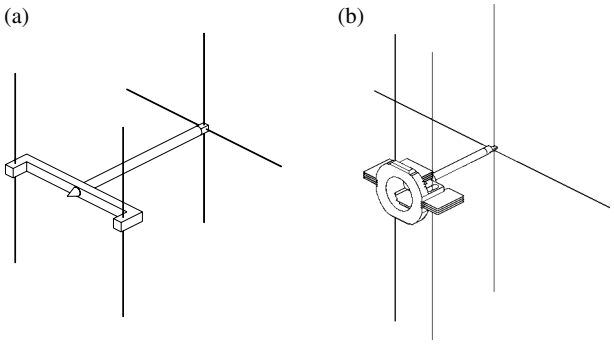

Figure 1. (a) Schematic suspension with three parallel fibres and one orthogonal fibre constraining the carrier to two degrees of freedom of motion: the probe tip can translate in a plane defined by the three attachment points, but cannot rotate. (b) View of carrier with capacitor armatures as constructed. To give an idea of scale, the distance from the tip to the rotation centre is 30 mm and the length of the four fibres is 80 mm.

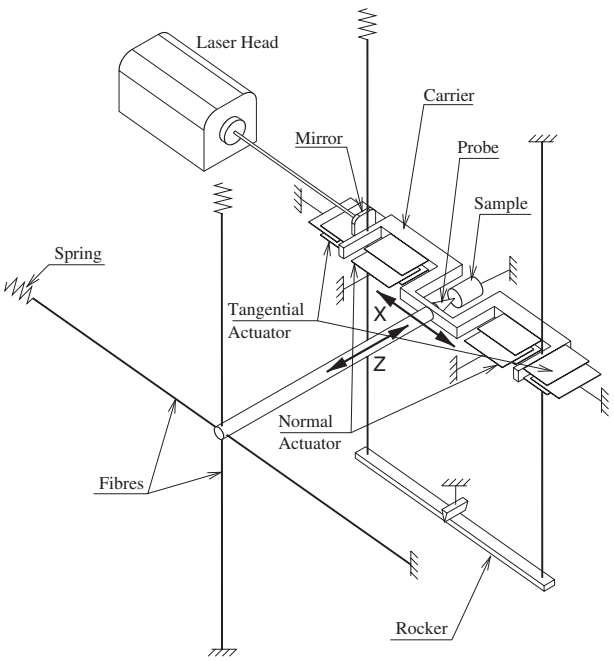

Figure 2. There is a balanced unipolar actuator acting in the normal direction, and a differential bipolar actuator in the lateral direction. The precise guidance allows the use of inteferometry to measure lateral displacements.

Precise guidance allowed us to use interferometry directly since a mirror attached to the carrier has a nearly fixed orientation. The geometry of the realized carrier is shown in figure 1(b). With 30 mm between the probe and the rotation centre, the displacement error in the normal direction is about 0.0167 nm for a tangential movement of 1 μm. A stiffness of 20 N m^{-1} (typical tuning) yields a normal force error of 0.33×10^{-9} N. By design, the inertial coefficients are close in the normal and tangential directions (about 10^{-3} kg).

Figure 2 shows schematically the elements of the system seen from the back. In the normal direction z, a unipolar actuator is divided into two sections in order to provide a normal force component coinciding with the tip. They are represented side by side in the figure for clarity, but

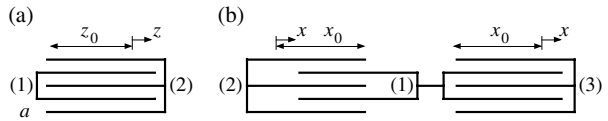

Figure 3. (a) Unipolar comb actuator. (b) Differential bipolar comb actuator.

in the constructed instrument, the two sections are stacked vertically. In the tangential direction x, the force is given by a bipolar differential actuator. The adjustable tension in each fibre allows for tunable compliance. The tension in the two front fibres is equalized by a rocker mechanism, eliminating spurious torque.

The geometry of the carrier (figure 1(b)) and of the capacitors was so designed that its centre of mass, the point where the electrostatic forces act, as well as the point where the elastic forces act, all coincide with the location of the junction under test, eliminating all static and dynamic couplings. Thus, denoting the tangential displacement by x and the normal displacement by z, the dynamics of the system is well described by two decoupled second order differential equations involving forces acting at the junction:

$$F_\mathrm{t} = m_\mathrm{t}\ddot{x} - a_\mathrm{t} - k_\mathrm{t}x - b_\mathrm{t}\dot{x}, \qquad F_\mathrm{n} = m_\mathrm{n}\ddot{z} - a_\mathrm{n} - k_\mathrm{n}z - b_\mathrm{n}\dot{z}. \tag{1}$$

F_t and F_n are the measured tangential and normal components of the force experienced by the junction, $m_\mathrm{t}\ddot{x}$ and $m_\mathrm{n}\ddot{z}$ are decoupled inertial terms, a_t and a_n are independently specified by the actuators, $k_\mathrm{t}x$ and $k_\mathrm{n}z$ are two known forces due to the compliance of the suspension, and $b_\mathrm{t}\dot{x}$ and $b_\mathrm{n}\dot{z}$ are viscous damping terms.

2.2. Electrostatic comb actuators

Comb actuators generally produce a force which is quadratically related to the voltage applied. This complicates device calibration because the incremental change of force depends on the operating point.

Consider a unipolar actuator as in figure 3(a), with a guided moving armature (1) meshing with a fixed armature (2). Given the electric potentials v_1 and v_2 of the armatures, the electrostatic energy is

$$E = \tfrac{1}{2}(c_{11}v_1^2 + c_{22}v_2^2 + 2c_{12}v_1v_2), \tag{2}$$

where the c_{ij} represent capacities. Ignoring the boundary effects, the capacity of any one pair of armatures is $\epsilon_0\epsilon_\mathrm{r}l_\mathrm{n}z_0/a$, where ϵ_0 is the permittivity of vacuum, ϵ_r the relative permittivity of air, l_n and z_0 represent the length and width of the armatures' opposing surfaces, and a the gap between them. Calling z the displacement of the moving armatures, N_n the number of gaps and posing $c_\mathrm{n} = (N_\mathrm{n}\epsilon_0\epsilon_\mathrm{r}l_\mathrm{n})/a$ gives

$$c_{11} = c_{22} = c_{12} = c_\mathrm{n}(z_0 + z). \tag{3}$$

The actuator force is $\partial E/\partial z = \frac{1}{2}c_\mathrm{n}(v_1^2 + v_2^2 + 2v_1v_2)$. Here, v_1 is assigned to a fixed voltage, and v_2 is assigned to an input control voltage v_n, so that the normal force produced by the actuator is

$$a_\mathrm{n} = c_\mathrm{n}(\tfrac{1}{2}v_1^2 + \tfrac{1}{2}v_\mathrm{n}^2 + v_1v_\mathrm{n}). \tag{4}$$

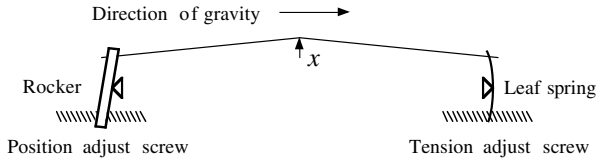

Figure 4. Deformation and loading of suspension fibre.

In the tangential direction, a novel bipolar differential electrostatic actuator was used to linearize the response and simplify calibration (see figure 3(b)). It has a guided moving armature (1) and two fixed armatures (2) and (3). Given the three voltages v_1, v_2, v_3, the electrostatic energy is

$$E = \tfrac{1}{2}(c_{11}v_1^2 + c_{22}v_2^2 + c_{33}v_3^2 + 2c_{12}v_1v_2 + 2c_{13}v_1v_3 + 2c_{23}v_2v_3). \tag{5}$$

Posing $c_\mathrm{t} = (N_\mathrm{t}\epsilon_0\epsilon_\mathrm{r}l_\mathrm{t})/a$ to reflect the geometry of the actuator, given the displacement x,

$$c_{11} = 2\,c_\mathrm{t}\,x_0, \qquad c_{22} = c_{12} = c_\mathrm{t}\,(x_0 - x), \qquad c_{33} = c_{13} = c_\mathrm{t}\,(x_0 + x), \qquad c_{23} \approx 0. \tag{6}$$

The actuator force is $\partial E/\partial x = \frac{1}{2}c_\mathrm{t}(-v_2^2 + v_3^2 - 2v_1v_2 + 2v_1v_3)$. Controlling the voltages so that v_2 and v_3 are opposites of each other, assigning them to a control voltage such that $v_3 = v_\mathrm{t}$ and $v_2 = -v_\mathrm{t}$, and fixing v_1, yields an actuator force equal to

$$a_\mathrm{t} = 2c_\mathrm{t}v_1v_\mathrm{t}. \tag{7}$$

Thus, the force produced is proportional to v_t. The voltage v_1 may also be used to adjust the actuator constant.

2.3. Elastic forces

Figure 4 shows the principle of the positioning and tensioning mechanism. The fibres are attached at one end to a positioning mechanism and at the other to an adjustable leaf spring that allows the tension to be set independently. The elastic forces due to carrier deflection result from the deformation of the tensioning leaf springs, from the fibre deformation, and from the suspended mass subject to gravity. It can be shown that the force arising from fibre deformation is orders of magnitude smaller than that arising from the other terms, and hence can be neglected. The tensions in the two front fibres are equal because they are on the same load path created by the rocker mechanism (figure 2). For small angles, the stiffness of the suspension in the tangential direction is $k_\mathrm{t} = (4T_\mathrm{t} - mg)/l_0$, where T_t is the tension in the fibres, mg the weight of the carrier that they support, and l_0 their half length. In the normal direction, the stiffness of the crossed back fibres having tension T_n adds to that of the front fibres, but almost no mass is supported, so $k_\mathrm{n} = k_\mathrm{t} + 4T_\mathrm{n}/l_0$. The stiffnesses can be independently set by adjusting T_n and T_t, according to the application. For most tunings, the suspension design achieves a compliance ratio of at least 1000 between the free and the constrained directions.

Leaf springs have a stiffness which depends on deflection. The arrangement has the effect of decoupling the compliance of the leaves from the displacements of the carrier. Call d the leaf deflection needed to create a tension T, and Δd

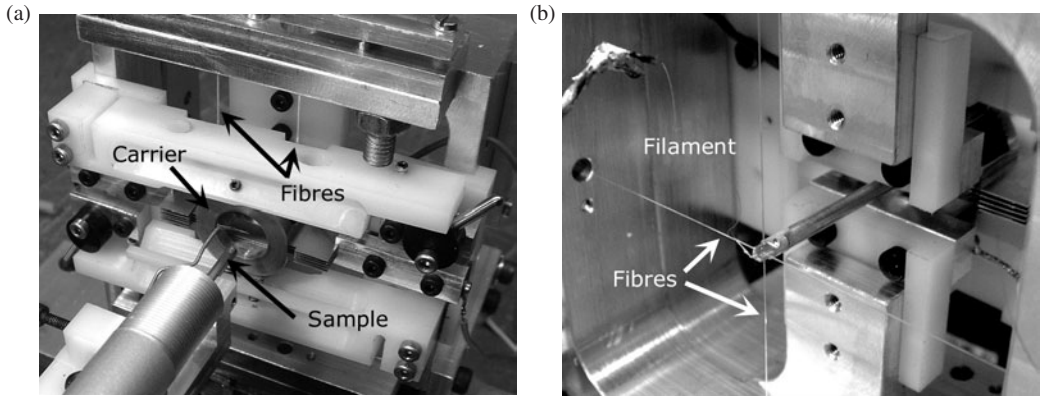

Figure 5. (a) View of instrument with microscope, the viewing mirror, and the sample moved back. The probing tip inside the carrier's cavity can be viewed with the microscope to monitor the contact between the sample and the probe. The two front glass fibres may be seen but are partially hidden by the locking mechanism used for transport and tip mounting. (b) At the back of the frame, the two crossing fibres constrain the carrier stem. The electrical grounding filament can also be seen.

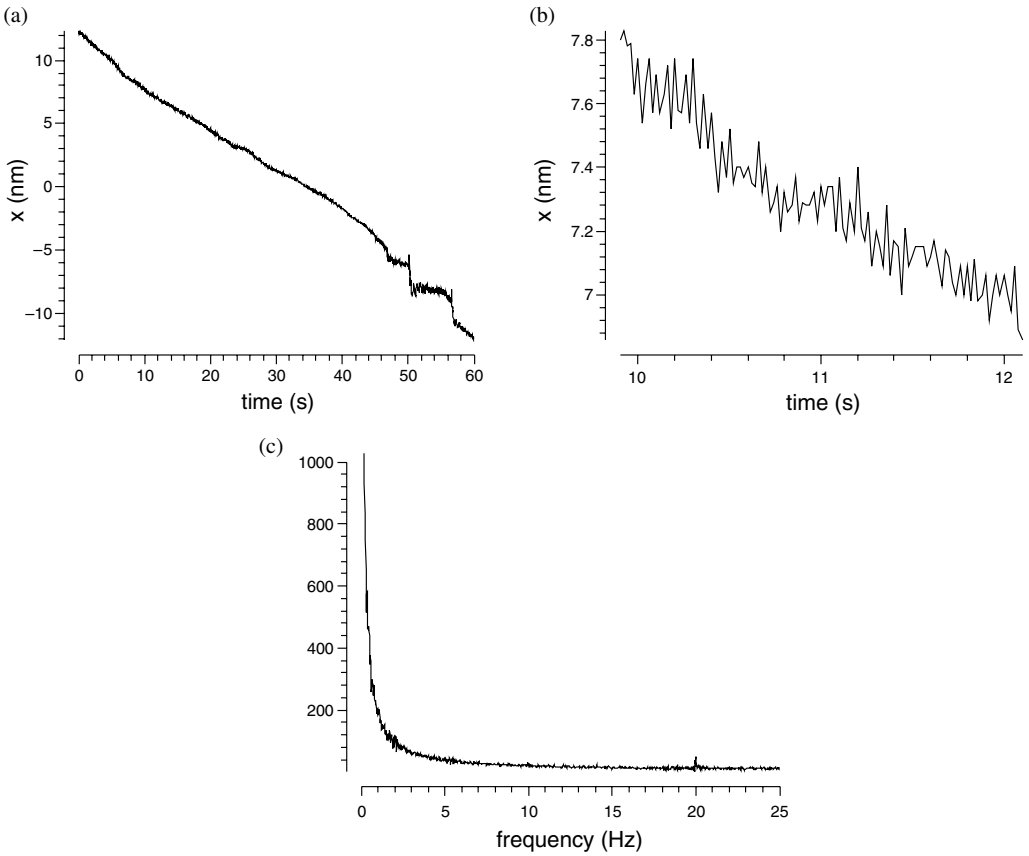

Figure 6. (a) Measurement made with the junction at rest. (b) Enlarged view of the signal from time 10 to 12 s. (c) Power spectrum below 25 Hz.

the incremental leaf deflection due to carrier displacement: $T = k_{\text{leaf}}(d + \Delta d)(d + \Delta d)$. By geometry, Δd is of the same order as x or z. If the leaf is selected so that $\Delta d \ll d$, then T is nearly constant, and so is the suspension compliance.

2.4. Calibration

From the mass of the moving part and from its displacement, the stiffnesses were found by measuring the natural frequencies in the tangential and normal directions. For the particular tuning used in section 3, the measured natural frequencies were 7.008 and 11.05 Hz corresponding to 3.5 and 8.7 N m^{-1} in the tangential and normal directions, respectively. The actuators were then calibrated. The result of calibration for the tangential bipolar actuator was $a_{\text{t}} = 1.30 \times 10^{-6} v_{\text{t}}$. The coefficient of the unipolar actuator acting in the normal direction could be known only approximatively. The maximum tangential force was ± 0.2 mN. Forces could be modulated as finely as permitted by the driving voltages. This is limited in the present realization by the resolution of the 16-bit digital-to-analogue converters used in the prototype.

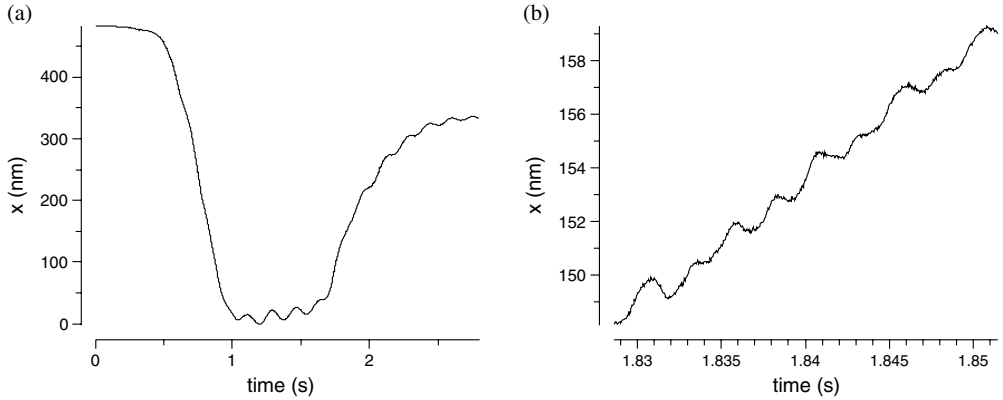

Figure 7. Mica–mica junction. (a) Response to a periodic tangential force over a period of about two seconds. (b) Same data, but zoomed-in by a factor of two orders of magnitude from time 1.83 to 1.85 s (raw measurements).

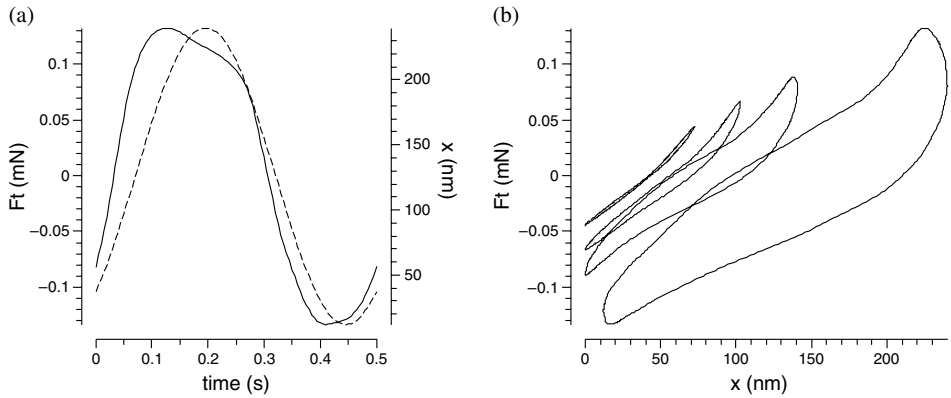

Figure 8. (a) Time domain recording of large scale hysteresis for one normal force (dashed curve: tangential force; solid curve: tangential displacement). (b) Four loops as displacement–force phase plots with the same tangential force but different normal forces. $F_c = 50$ Hz.

2.5. Construction

The device was composed of an aluminium frame supporting the fibre tensioning mechanisms and the fixed actuator armatures (figure 5(a)). Much care was exercised to minimize hysteresis by careful fibre attachment design and by using long glass fibres (0.13 mm diameter) that underwent very little strain. The sample was supported by micrometric translation and rotary stages for accurate positioning. Electrical connection to the moving carriage was provided by a tungsten incandescent lamp filament attached near the centre of rotation to minimize its movement and hence the perturbations it might introduce (figure 5(b)).

Actuator voltages v_n, v_t, and $-v_t$ were set by three precision high voltage operational amplifiers driving the actuators via low-pass passive filters (±200 V, 1 kHz cut-off). These amplifiers were driven by 16-bit analogue-to-digital converters. The armature voltages were also converted with 16-bit resolution via precision resistor bridges. It is these voltages that were used to measure the force supplied by the actuators, once they were calibrated.

2.6. Scaling

Since future versions of similar instruments could be greatly miniaturized, it is interesting to examine the factors that affect the measurement range as a function of scale. Recall that the instrument obeys two decoupled equations of the form

$$F = m\ddot{x} - a - kx - b\dot{x}, \tag{8}$$

where the force F is the quantity to be measured, and where the other terms are known from calibrated quantities and displacement measurements. The instrument can be operated in three modes defined by the natural frequency $f_0 = 1/2\pi\sqrt{k/m}$.

In the quasi-static mode I below f_0, the elastic term kx in equation (8) dominates. Therefore, the force supplied by the actuators must balance both the force to be measured and the elastic force due to deflection. In the resonant mode II at f_0, the elastic term kx and the inertial term $m\ddot{x}$ cancel each other. The sensitivity is only a function of damping which is very low: the force supplied by the actuators equates almost exactly to the force to be measured. In the third mode III above f_0, the inertial term $m\ddot{x}$ dominates, rising quadratically with the operating frequency. Mode III is useful for measurements at high velocity or with tunings with high compliance. Thus, any instrument of this kind is governed by design tradeoffs which are different in each mode.

In mode I, the maximum scanning distance x_M, the suspension stiffness k, and the actuator saturation a_M are related through $x_M = ka_M$, an expression that defines the basic operational range. In mode III, the tradeoff involves scanning distance, inertia, and actuator saturation. For a

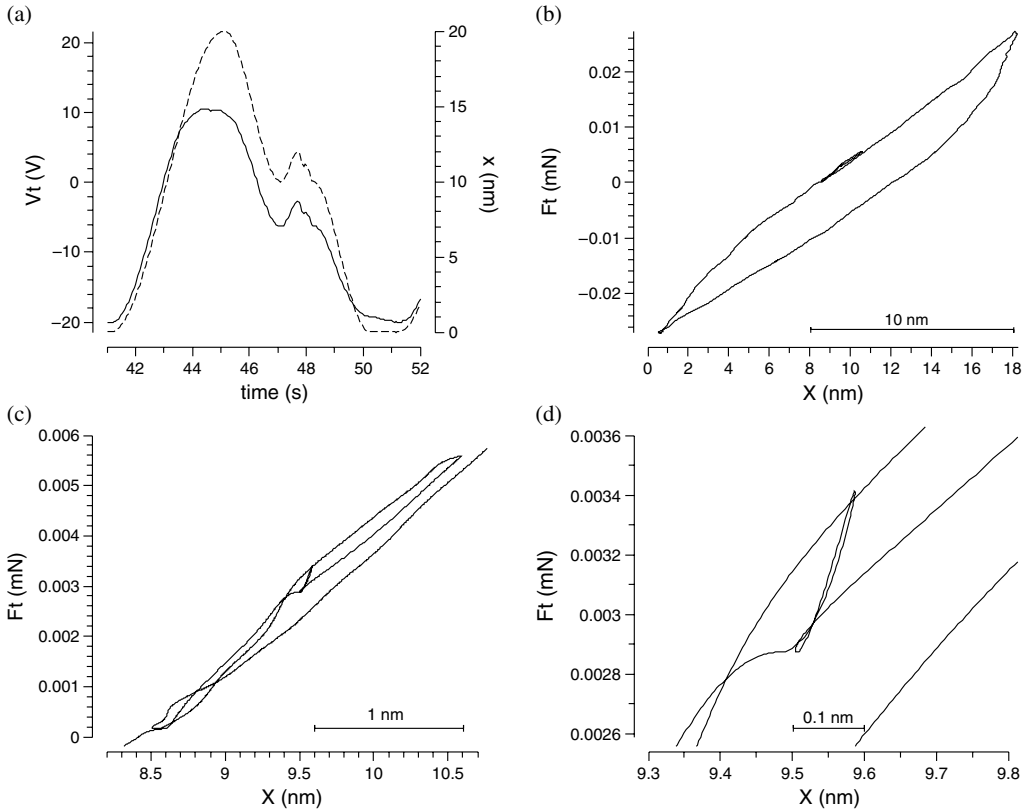

Figure 9. Small scale hysteretic behaviour test of a steel junction. (a) Tangential voltage (dashed curve) and corresponding displacement (solid curve). (b) Major hysteresis loop (18 nm), (c) minor loop (2 nm), (d) second order minor loop (70 pm). $F_c = 8.3$ Hz.

Table 1. Maximum values of static and dynamic terms for each measurement example. In all cases, the inertial term is overestimated since these values were computed by finite difference from the unfiltered displacement signal. The same holds for the damping term. In addition, the value used for b was estimated from the free response at large velocities. This value is probably much lower during measurements.

Figures	Max a_t (N)	Max $[kx]$ (N)	Max $[b\dot{x}]$ (N)	Max $[m\ddot{x}]$ (N)
5(a)	2.2×10^{-5}	7.1×10^{-7}	1.8×10^{-7}	9.5×10^{-6}
5(b)[a]	2.0×10^{-6}	2.5×10^{-7}	0.7×10^{-7}	2.0×10^{-6}
6(b)	1.3×10^{-4}	3.3×10^{-7}	1.2×10^{-7}	7.5×10^{-8}
7(b)	2.8×10^{-5}	1.7×10^{-8}	7.0×10^{-10}	1.0×10^{-9}
7(c)	6.0×10^{-6}	1.0×10^{-8}	5.0×10^{-10}	1.0×10^{-9}
7(d)	3.4×10^{-6}	7.3×10^{-9}	3.5×10^{-10}	1.0×10^{-9}
7(d)[b]	0.7×10^{-6}	1.0×10^{-9}	8.0×10^{-10}	1.0×10^{-9}
8(a) and (b)[c]	1.2×10^{-5}	1.1×10^{-5}	0.8×10^{-5}	1.4×10^{-5}
8(c) and (d)[d]	2.2×10^{-6}	2.1×10^{-6}	0.5×10^{-6}	0.1×10^{-6}
9(a)	4.5×10^{-5}	2.9×10^{-6}	0.7×10^{-6}	3.7×10^{-8}
9(b) and (c)	4.5×10^{-5}	0.5×10^{-6}	4.0×10^{-8}	2.5×10^{-9}

[a] Rough estimate of the actuator force.

[b] Indicates difference between maximum and minimum values in the minor loop.

[c] At large displacement, almost all the actuator force is used to balance the elastic term.

[d] Figure compensated for the elastic term.

maximum scanning distance x_M, the upper frequency limit is $1/2\pi\sqrt{a_M/(mx_M)}$.

These factors vary as a function of the scale defined by a characteristic length l. The meso-scale instrument presently constructed is such that $l \sim 10^{-2}$ m, $m \sim 10^{-3}$ kg, $b \sim 10^{-1}$ N s m^{-1} (in air), $a_M \sim 10^{-4}$ N, $x_M \sim 10^{-5}$ m, and $k \sim 10$ N m^{-1}; thus, $f_0 \sim 10$ Hz.

We now can estimate the performance of a system that would be scaled down, say by two orders of magnitude to the level of a MEMS device ($l \sim 10^{-4}$ m). The moving mass would vary as l^3. At a smaller scale, the suspension fibres would be replaced by beams. Unlike the meso-scale device reported here in which stiffness can be tuned, the stiffness would then be dominated by beam deflection which would decrease linearly with l. So the resonance frequency would scale as $\sqrt{k/m} \propto \sqrt{l/l^3} = 1/l$. A micro-scale device could be predicted to resonate at 1 kHz. The actuator meshing length would decrease with l but the gap distance would decrease with l too, so these two factors cancel each other. Based on the Paschen law and on data reported for MEMS devices [14, 15], the maximum voltage could be invariant with scale, so the maximum actuator force would also be invariant. In mode I, the maximum scanning distance would scale with l. For a MEMS scale device, this would give $x_M \sim 10^{-7}$ m. In mode III, for the same scanning distance, the frequency limit due to actuator saturation would vary as $\sqrt{a_M/(mx_M)} \propto l^{-2}$. For a MEMS scale device this would give a maximum frequency of 100 kHz.

3. Measurements examples

The system was placed in an enclosed 2 ton optical table pneumatically isolated from the ground and protected with a heavy hood from acoustic vibrations. An additional elastic

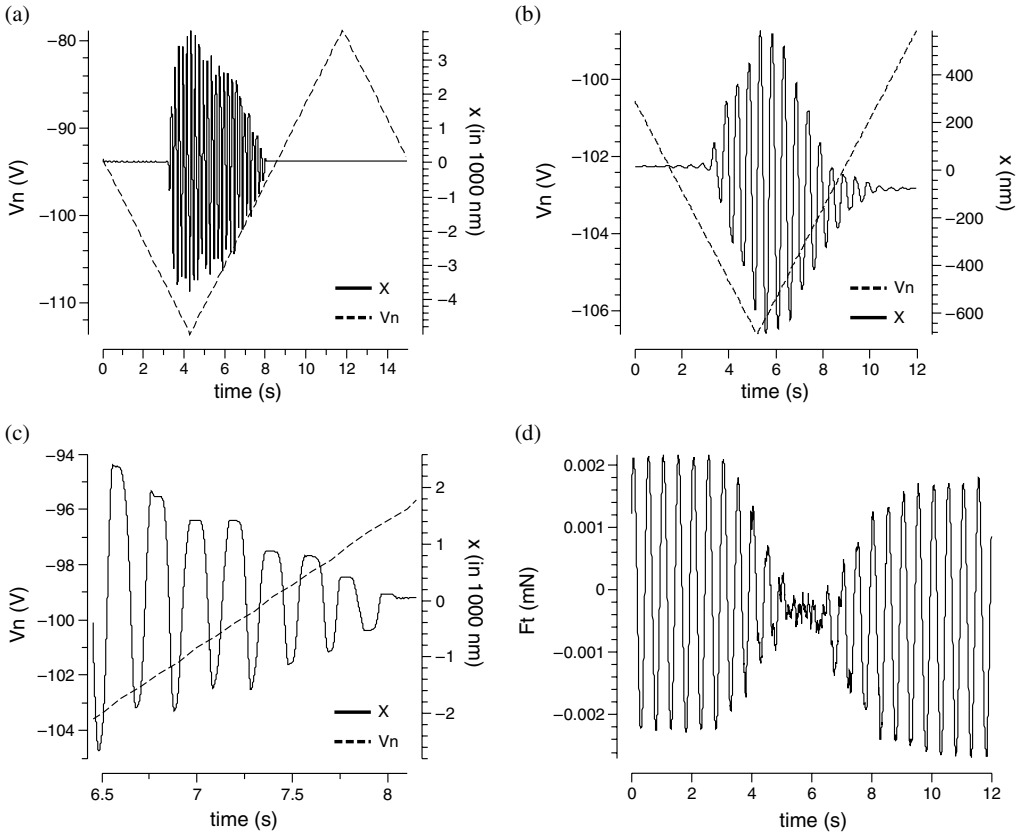

Figure 10. (a) and (b) Effect of normal force for displacements at two length scales. (c) Enlargement of (a) when the normal force becomes large. (d) The tangential friction force drops to a small value when the tangential displacement is the largest in (b). $F_c = 8.3$ Hz.

suspension made of six 1 m latex hoses was used to further reduce the noise level. The additional suspension had a resonance at 2 Hz and its free oscillations decayed in 2 s.

After a stabilization period, measurements were then made with the carriage freely suspended. There were at least three sources of noise: mechanical vibration and sound, the interferometer intrinsic noise and thermal drift. A very low damping coefficient of 0.05 N s m^{-1} could be estimated. To evaluate the noise floor, displacement recordings were made with the junction at rest (figure 6). The interferometer noise was in the range 0.1–0.2 nm with a component probably due to thermal drift, because the thermal expansion term of the supporting structure was of the order of 1.6 nm/thousandth of degree centigrade. These tests indicated that indeed details at subnanometre scale can be measured.

In the measurements reported below, the force and displacement signals were frequency-limited by transforming them in the Fourier domain, truncating the spectrum below a given frequency F_c, and then reconstructing the time-domain signal (thus preserving the phase information). The cutoff frequency is indicated in the captions of the experimental figures.

Measurements were made for two cylindrical mica surfaces contacting orthogonally and for a sharp steel point interacting with a polished flat steel surface. Friction forces were measured for displacements in the range of 0.1–10 000 nm for various kinds of force trajectories. The measurements where all made in mode I. For each example, table 1 collects the relative importance of the static and dynamic terms. In most cases, displacements, velocities, and accelerations were sufficiently low to identify the actuator force with the force experienced at the junction. A selection of results, here briefly discussed, show a variety of effects and phenomena.

3.1. Mica on mica sticking and sliding friction

Samples were made of sheets of mica each bonded to two steel half cylinders of 1.0 mm radius. They were touching at a right angle. A sinusoidal signal of period 2.5 s was applied tangentially. The resulting displacement is shown in figure 7(a) measured at a rate of 35 000 samples s^{-1}. After a sliding initial transient until time 1.0 s, the contact comes to rest while oscillating with period 0.2 s until time 1.75 s, probably because of the compliance in the contact. It then breaks away to come to rest again with a similar oscillatory behaviour. Zooming-in inside a portion of the sliding motion reveals very small oscillations with an amplitude of about one nanometre (figure 7(b)).

3.2. Large scale hysteresis as a function of normal force

Figure 8 shows four force–displacement hysteresis loops obtained with the same periodic tangential force applied to the mica–mica junction, but with four different normal forces. Figure 8(a) show one such measurement in the time domain. Figure 8(b) shows the four phase diagrams of friction force

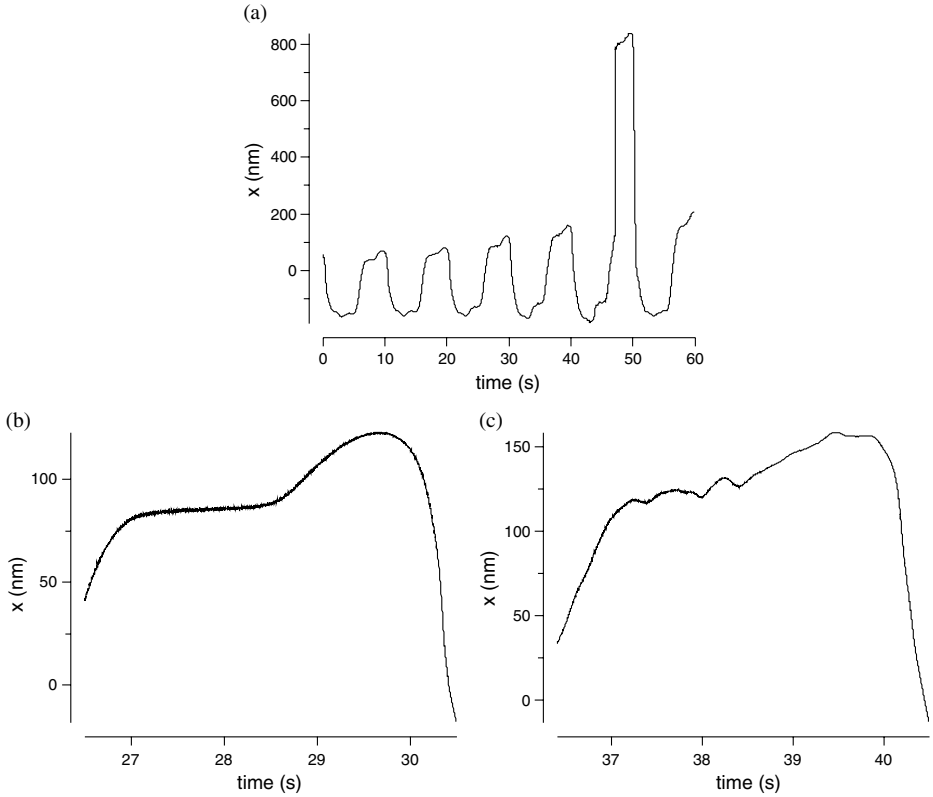

Figure 11. (a) The steel junction experiences a periodic tangential force. While the displacement extrema are normally smooth, for example (b) from time 27 to 30 s, the last extremum (c) before junction failure leading to slipping is extremely active during time 37 to 30 s (raw measurements).

versus displacement. Lack of calibration prevented us from knowing exactly the magnitude of the normal force component.

3.3. Hysteresis at various scales

Figure 9(a) shows a tangential force trajectory composed of three sinusoidal arcs of decreasing amplitude, each a tenth the size of the previous one. This was used to examine the hysteretic behaviour of the same junction at three length scales, creating three loops each one-tenth the size of the previous. The same data are shown in figures 9(b)–(d) as phase diagrams. A sharp increase in junction stiffness would typically be observed for hysteresis loops at subnanometre scale, as seen in smallest minor hysteresis loop in figure 9(d).

3.4. Effect of the normal force

The influence of the normal force on junction behaviour is shown in figures 10(a) and (b) for displacements at two different scales. A sharp steel point interacted with a polished steel flat surface with a sinusoidal tangential actuator force. The dashed lines represent the voltage applied to the normal actuator. We could not know the force magnitude for lack of calibration, but the actuator response was linearized while operating around 100 V.

This indicates an inverse relationship between the normal force and the tangential displacement. Many details are contained in figure 10(a) with large tangential displacements of up to ± 4 μm. One of them is shown in figure 10(c) where the tangential displacement becomes very small. Figure 10(b) shows a similar experiment, but at a smaller length scale with displacements of about ± 0.5 μm. Figure 10(d) shows how the tangential force vanishes when the contact is broken. In plotting the tangential force, the elastic term was not neglected since the displacement is large (see table 1).

3.5. Transition to sliding

Figure 11(a) shows the same junction experiencing a sinusoidal tangential force of period 10 s. The bond progressively fails before a transition from sticking to sliding. Signs of failure slowly gain amplitude in the cycles prior to a transition to sliding at time 48 s, as seen in figures 11(b) and (c), for times 27–30 and 37–40 s respectively. After failure at time 48 s, the junction slips by 600 nm and then slips back to 'bond' again exactly at the location of failure. The tangential displacement had a varying amplitude although the force experienced by the junction was periodic.

4. Discussion

The FFS is distinct from previous designs in several aspects. Electrostatic forces are used instead of bending stresses to balance the force experienced by a junction. The probe is mounted on a carrier suspended by fibres arranged to constrain its movement to two degrees of translational freedom with a high degree of decoupling and linearity of the compliant behaviour. A quasi-ideal kinematic guidance, a new electrostatic actuator responding linearly to voltage, and the use of interferometry yield a large range of calibrated

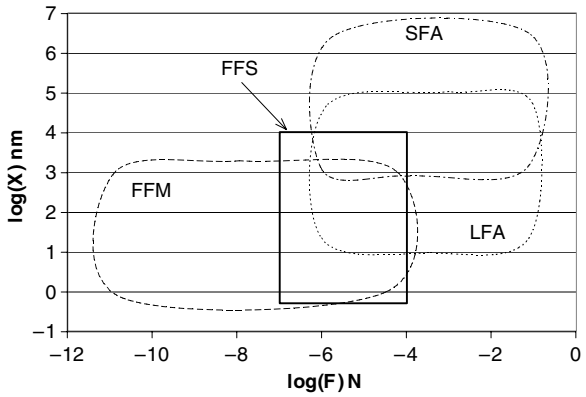

Figure 12. Relative achievable ranges with the FFM, the LFA, the SFA, and the present realization of the FFS.

measurements both in force and displacement within a single-stage design.

Based on [16] and [9], it is possible to situate the performance of the present realization of the friction force scanner using figure 12 where the lateral force apparatus LFA [9], the surface force apparatus SFA [8], and the friction force microscope FFM [7] are mapped in terms of the range of forces and displacements they can achieve. It should be noted that the present realization of our instrument is limited in the low range by the use of 16-bit converters. It is likely that one or two additional orders of magnitude of resolution could be achieved with higher resolution control on the voltages applied.

The present prototype has limitations that could be overcome with improved fabrication, while retaining the same design principles. Chief among possible improvements would be the introduction of a differential actuator in the normal direction as well as in the tangential direction. This would permit accurate, calibrated determination of the normal force. This along with a second PODS interferometer would allow for the complete determination of the behaviour of a junction.

Another important improvement would be the reduction of the mass of the carrier. It is presently machined out of magnesium and supports aluminium foil capacitor armatures. Electric discharge machining would make it possible to manufacture the carrier and the armatures from one single part, reducing the moving mass by an order of magnitude. Alternatively, MEMS fabrication techniques could yield further reduction of mass, but it is not clear how the fibre suspension could be realized. It is, however, likely that at small scales, the load of gravity can be ignored and the tension in the fibres set to zero. This is equivalent to replacing them with beams attached to the supporting structure at one end only, making the MEMS option more attractive.

Acknowledgments

We would like to thank Peter Grutter from McGill University and Ian Sinclair from MPBT for helpful comments. The assistance of MPB Technologies Inc. in providing laboratory space for the work, an optical table, and the PODS measurement system, is gratefully acknowledged.

The first author would like to thank Université Paul Sabatier and the Laboratoire d'Analyse et d'Architecture des Systèmes for granting a sabbatical leave. Additional funding for this research was provided by an operating grant from NSERC, the Natural Science and Engineering Council of Canada to the second author.

References

[1] Sokoloff J B, Krim J and Widom A 1993 Determination of an atomic-scale frictional force law through quartz crystal microbalance measurements *Phys. Rev.* B **48** 9134–7

[2] He G, Müser M H and Robbins M O 1999 Adsorbed layers and the origin of static friction *Science* **284** 1650–2

[3] Gerde E and Marder M 2001 Friction and fracture *Nature* **413** 285–8

[4] Bushan B and Danvadate C 2000 Thin-film and adhesion studies using atomic force microscopy *J. Appl. Phys.* **87** 1201–10

[5] Caroli C and Nozières P 1998 Hysteresis and elastic interactions of microasperities in dry friction *Eur. Phys. J.* B **4** 233–46

[6] Hölscher H, Schwarz U D and Wiesendanger R 1996 Simulation of a scanned tip on NaF(001) surface in friction force microscopy *Europhys. Lett.* **36** 19–24

[7] Mate c M, McClelland G M, Erlanson R and Chiang S 1987 Atomic-scale friction of a tungsten tip on a graphite surface *Phys. Lett.* **59** 1942–5

[8] Israelachvili J, McGuiggan P, Gee M, Homola A, Robbins M and Thompson P 1990 Liquid dynamics in molecularly thin films *J. Phys.: Condens. Matter* **2** SA89–98

[9] Hendriks C P and Vellinga W P 2000 Quantitative measurement of sliding friction dynamics at mesoscopic scales: the lateral force apparatus *Rev. Sci. Instrum.* **71** 2391–402

[10] Joyce S A and Houston J E 1991 A new force sensor incorporating force-feedback control for interfacial force microscopy *Rev. Sci. Instrum.* **62** 710–5

[11] Jarvis S P, Tokumoto H, Yamada H, Kobayashi K and Toda A 1999 An alternative method for the activation and measurement of lateral forces using magnetically controlled atomic force microscopy *Appl. Phys. Lett.* **75** 3883

[12] Feige V K S and Balk L J 2003 Calibration of a scanning probe microscope by the use of an interference-holographic position measurement system *Meas. Sci. Technol.* **14** 1032–9

[13] Charette P G, Hunter I W and Brenan J H 1992 A complete high performance heterodyne interferometer displacement transducer for microactuator control *Rev. Sci. Instrum.* **63** 241–8

[14] Legtenberg R, Groeneveld A W and Elwenspoek M 1996 Comb-drive actuators for large displacements *J. Micromech. Microeng.* **6** 320–9

[15] Ono T, Sim D Y and Esashi M 2000 Micro-discharge and electric breakdown in a micro-gap *J. Micromech. Microeng.* **10** 445–51

[16] Carpick R W and Salmeron M 1997 Scratching the surface: fundamental investigations of tribology with atomic force microscopy *Chem. Rev.* **97** 1163–94